








RESEARCH ARTICLE | DECEMBER 04 2023

Production of 13.5 nm light with 5% conversion efficiency from 2 μm laser-driven tin microdroplet plasma

Special Collection: [Plasma Sources for Advanced Semiconductor Applications](#)Y. Mostafa ; L. Behnke ; D. J. Engels ; Z. Bouza; J. Sheil ; W. Ubachs ; O. O. Versolato  *Appl. Phys. Lett.* 123, 234101 (2023)<https://doi.org/10.1063/5.0174149>

Articles You May Be Interested In

The spectrum of a 1- μm -wavelength-driven tin microdroplet laser-produced plasma source in the 5.5–265.5 nm wavelength range


AIP Advances (December 2021)

Fabrication of concave gratings by curved surface UV-nanoimprint lithography

J. Vac. Sci. Technol. B (September 2008)

Dependence of ion charge-energy emission from Nd:YAG-laser-produced plasma on laser intensity in the 0.4 – 40 $\times 10^{10}$ W/cm² range

Phys. Plasmas (August 2023)



Your One-Stop Shop for the Best Brands in Optics

- Extensive inventory with over 34,000 products available & 2,900 new products
- Fast shipping from our 9 distribution centres around the globe
- Bringing 80+ years of optical expertise to customers worldwide

Edmund
optics | worldwide

[Shop Now](#)

Production of 13.5 nm light with 5% conversion efficiency from 2 μm laser-driven tin microdroplet plasma

Cite as: Appl. Phys. Lett. **123**, 234101 (2023); doi: [10.1063/5.0174149](https://doi.org/10.1063/5.0174149)

Submitted: 28 August 2023 · Accepted: 15 November 2023 ·

Published Online: 4 December 2023



View Online



Export Citation



CrossMark

Y. Mostafa,^{1,2} L. Behnke,^{1,2} D. J. Engels,^{1,2} Z. Bouza,^{1,2} J. Sheil,^{1,2} W. Ubachs,^{1,2} and O. O. Versolato^{1,2,a)}

AFFILIATIONS

¹Advanced Research Center for Nanolithography, Science Park 106, 1098 XG Amsterdam, The Netherlands

²Department of Physics and Astronomy, and LaserLaB, Vrije Universiteit Amsterdam, De Boelelaan 1081, 1081 HV Amsterdam, The Netherlands

Note: This paper is part of the Special Topic: Plasma Sources for Advanced Semiconductor Applications.

^{a)} Author to whom correspondence should be addressed: o.versolato@arcnl.nl

ABSTRACT

We demonstrate the efficient generation of extreme ultraviolet (EUV) light from laser-produced plasma (LPP) driven by 2 μm wavelength laser light as an alternative for 10 μm CO₂ gas LPP currently employed in EUV lithography machines for high-volume manufacturing of semiconductor devices. High conversion efficiencies of laser light into “in-band” EUV photons up to 5.0% are achieved by homogeneously heating the plasma that is laser-generated from preshaped tin microdroplet targets. Scaling the laser pulse duration, spot size, and intensity yields a high in-band EUV energy output of up to 12.5 mJ. The EUV emission source size is studied under a similar parameter range and is shown to match typical etendues of EUV optic columns. Our findings make 2 μm LPP a particularly promising candidate to power future EUV nanolithography.

© 2023 Author(s). All article content, except where otherwise noted, is licensed under a Creative Commons Attribution (CC BY) license (<http://creativecommons.org/licenses/by/4.0/>). <https://doi.org/10.1063/5.0174149>

Today's most advanced nanolithographic machines utilize extreme ultraviolet (EUV) light to “print” ever smaller features on chips.^{1,2} EUV light is generated by laser-produced tin plasma sources driven by 10.6 μm wavelength CO₂ gas lasers.^{3,4} Laser light impacting tin microdroplets generates plasmas that contain highly excited, multiply charged ions that emit EUV light primarily in the 2% “in-band” region around 13.5 nm.^{5–8} The generated EUV light can be collected using concave multilayer reflective optics enabling the lithographic process.⁷ The performance of laser-produced plasmas (LPP) is assessed in multiple ways, primarily by the conversion efficiency (CE) of laser light into in-band light emitted in the 2π hemisphere facing the laser. Current nanolithographic machines using CO₂ lasers have a CE of approximately 5%–6%, emitting several 10 mJ of in-band radiation per pulse.^{4,9} In addition to CE, the size of the emitting area is important to assess the overall efficiency of the LPP. Ideally, this source size is matched to the etendue of the optics, with typical values ranging 1–3.3 mm² sr depending on specifics of the lithography apparatus.^{10,11}

Plasmas generated by 10 μm lasers require complex tin target preparation and shaping to achieve high CE.^{9,11–14} Combined with the

low wall-plug efficiencies of 10 μm gas lasers, this has motivated research into plasmas driven by shorter wavelength, highly efficient solid-state lasers to strongly accelerate in recent years.^{15–21} Radiation-hydrodynamic simulations have shown promise of high CE plasma sources driven by 2–5 μm lasers¹³ without the need for complex target shaping. Given the maturity of 1.064 μm solid-state laser technology, and the strong progress in 1.88 μm laser development,^{20,21} studies have focused on tin plasmas generated by 1- and 2 μm laser light.^{15,19,22–24} Relatively low CEs have been recorded for 1 μm plasmas due to re-absorption losses in dense plasma media,^{16,18} given the relation $n \sim \lambda^{-2}$ between drive laser wavelength λ and n , the critical plasma density.³ Consistently, twofold higher CEs have been found using 2 μm laser light, under otherwise comparable conditions.^{16–18} However, the experiments using focused 2 μm light did not yield CE values competitive with the CO₂ state-of-the-art, with maximum CEs being limited to approximately 3%—and no information on 2 μm laser-driven source size is currently available. It was hypothesized^{17,25,26} that CE values could increase significantly if the plasma is heated homogeneously, i.e., in a manner that is constant spatially and temporally to generate a uniform

(optimum) temperature plasma. However, no direct experimental evidence for the $2\ \mu\text{m}$ case is yet available.

In this work, we present the high-efficiency operation of $2\ \mu\text{m}$ laser-produced plasmas, achieving up to $\text{CE} = 5\%$ using a simple two-pulse scheme. We demonstrate that the optimization of the laser's temporal and spatial profiles, as enabled by our recent laser development,²⁷ allows for future, high-performance EUV sources powered by $2\ \mu\text{m}$ laser technology. Scaling to high (up to 12.5 mJ) EUV pulse energies is demonstrated while maintaining a small emission size.

In our experiments, tin microdroplets are generated by streaming liquid tin through a nozzle within a vacuum chamber held at 10^{-6} mbar. A low energy $1\ \mu\text{m}$ wavelength “pre-pulse” laser preshapes the tin droplet into a flat target.^{3,17,28} A second, high energy $2\ \mu\text{m}$ “main-pulse” laser is later fired onto the tin target, generating an EUV emitting plasma.^{17,27} We control the target diameter (ϕ_T) impacted by the main-pulse by varying the delay time between pre-pulse and main-pulse, allowing for larger targets at longer delays. A schematic of the setup is shown in Fig. 1(a). The $2\ \mu\text{m}$ main-pulse used in this work is an in-house-built master oscillator power amplifier system

(10 Hz repetition rate) as described in our recent work.²⁷ The laser temporal profile is shaped into a uniform “box-shape” intensity as shown in Fig. 1(b). We control the pulse duration and vary it in the range 10–32 ns using a series of Pockels cells. We similarly control the spatial profile by scanning along the propagation of the laser beam and implementing various imaging configurations. The spatial radial average of the beam profile at the tin target is shown in Fig. 1(c) for two flat-top beam diameters of 67 and $144\ \mu\text{m}$. Shown also in Figs. 1(b) and 1(c) are the Gaussian beam profiles as studied in previous work,¹⁸ to be compared to the here-studied flat-top cases. The spatial profiles are shown in detail in Figs. 1(d)–1(f) for the $67\ \mu\text{m}$ flat-top, $144\ \mu\text{m}$ flat-top, and $120\ \mu\text{m}$ Gaussian beam, respectively.

To study the in-band emission, we place calibrated, EUV-sensitive photodiodes at angles 30° , 41° , 64° , 90° , and 114° with respect to the laser axis as shown in Fig. 1(a). The combined measurement of the EUV photodiodes results in the anisotropy corrected absolute total emission of EUV light. The conversion efficiency of laser light energy into 13.5 nm light emitted in the hemisphere toward the laser is calculated accordingly. The uncertainty in the CE value is calculated considering the uncertainties in the laser energy measurement (2%), calibrating the EUV photodiodes (6%), and the anisotropic fit used to extract the emission fraction into 2π (9% systematic uncertainty), as well as accounting for statistical errors. We study emission spectra in the range 5.5–25 nm using a transmission grating spectrometer, which we orient at 60° (cf. Bouza *et al.*²⁹). We additionally investigate the source emission area by acquiring images of the $13.5 \pm 1\%$ nm emission using a concave multilayer Mo/Si mirror in combination with an EUV-sensitive CCD (Greateyes BI UV1). This EUV imaging system is placed at 90° . Data presented are averages of 100–200 laser shots.

We observe an increasing CE for increasing target diameters for three main-pulse cases as shown in Fig. 2(a). The dashed lines are based on a CE scaling with the geometrical overlap of the main-pulse laser spatial profile [taken from Fig. 1(c)] with the tin target for the

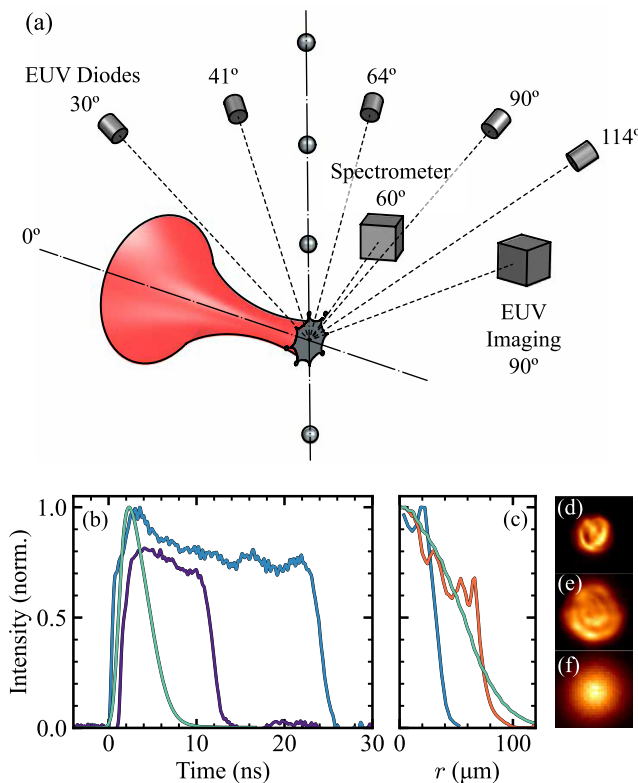


FIG. 1. (a) Overview of the experimental setup showing $2\ \mu\text{m}$ main-pulse impacting preformed tin targets. Five diodes are placed at angles 30° , 41° , 64° , 90° , and 114° with respect to the laser axis. EUV spectra are measured using a transmission grating spectrometer positioned at 60° . EUV emission profiles are imaged using a concave multi-layer mirror imaging system at 90° . For three different main-pulse diameter cases of $67\ \mu\text{m}$ flat-top (●), $144\ \mu\text{m}$ flat-top (○), and $120\ \mu\text{m}$ Gaussian (△), we show (b) the laser temporal profiles where a shorter pulse duration of $67\ \mu\text{m}$ flat-top (●) case is also presented, and (c) angularly averaged laser radial profiles and (d)–(f) showing the respective spatial intensity profiles.

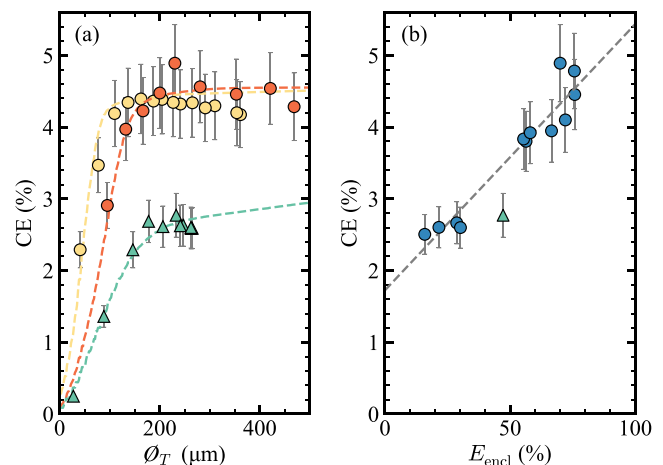


FIG. 2. (a) Scaling of CE with tin target diameter for three different main-pulse laser cases of $67\ \mu\text{m}$ flat-top (○), $144\ \mu\text{m}$ flat-top (●), and $120\ \mu\text{m}$ Gaussian (△). The dashed lines indicate the fit of the geometrical overlap of the beam and target areas. (b) Scaling of CE with energy enclosed within the flat-top (●) main-pulse beam's spatial FWHM. The dashed line is a trendline fit to the data.

three cases, with the amplitude as a free fit parameter following the approach of Schupp *et al.*¹⁸ We offset the geometrical overlap function along the x -axis by a common $21\text{ }\mu\text{m}$ [number taken from Fig. 4(c), consistent with simulations¹³] to account for plasma expansion, which enlarges the area where the beam is absorbed^{13,17} for pulse durations beyond several nanoseconds.^{18,30} These simple model curves closely match the experimental data. For the flat-top cases, the CE plateaus but at target diameters larger than the beam, as may be expected given that part of the laser energy is situated outside of the area set by the flat-top diameter. Figure 2(a) shows that flat-top pulses result in higher conversion efficiencies than the Gaussian one. This difference is attributed to the uniform heating of the LPP, resulting in a uniform temperature and emission within the 13.5 nm band across the plasma. Non-uniform illumination may overheat and underheat areas of the plasma, resulting in unwanted out-of-band emission.³¹ Underheated plasma regions may, moreover, lead to additional self-absorption.^{16,31,32} We note that there is no difference in the maximum obtained CE comparing the 67 and $144\text{ }\mu\text{m}$ flat-top cases. Schupp *et al.*²⁶ found that enlarging beam size negatively impacted CE when using $1\text{ }\mu\text{m}$ drive laser pulse due to increasing optical depth, in contrast with the current findings. This contrast is indicative of the lower plasma densities, and optical depth, of the $2\text{ }\mu\text{m}$ case leading to less self-absorption of the produced EUV light.¹⁶

Having understood the difference in obtainable CE between flat-top and Gaussian pulses in terms of illumination homogeneity, we next study the influence of beam intensity uniformity on the maximum CE. As a simple metric of uniformity, we use the energy enclosed within the 50% intensity contour of the spatial beam profile, denoted E_{encl} . Figure 2(b) shows optimal CEs under various

E_{encl} illumination cases, maintaining constant average intensity as is verified by comparing the emission spectra.¹⁷ The movement of the laser focusing lens enables scaling the beam spot size, moving from near-focusing conditions to and beyond the image plane [beam spot sizes can be found in Figs. 3(a) and 3(b)]. We observe a clear upward trend of CE with E_{encl} , indicating CE values beyond 5% may be achieved for perfectly uniform illumination. The highest conversion efficiency we observed within the studies contained in this paper is $5.0\% \pm 0.6\%$ when optimizing all parameters at optimum beam quality. We note that the Gaussian pulse case ($E_{\text{encl}} = 50\%$) undershoots the trend as expected from the aforementioned over- and underheating associated with the Gaussian profile, leading to significant self-absorption and out-of-band reemission.¹⁶

Having achieved CE values competitive with state-of-the-art CO₂-laser-driven industrial EUV light sources,^{4,9} we next focus on scaling toward higher EUV pulse energies while maintaining high CE. For nanolithographic applications, EUV emitting plasmas typically emit several 10 mJ of in-band radiation.^{4,9} To achieve similar emission energies, we investigate the output EUV energy scaling with respect to three laser parameters: spot diameter on tin target (ϕ_L), intensity (I), and pulse duration (τ_L). Target size is maintained much larger than the beam size, guaranteeing complete geometric overlap. In Figs. 3(a) and 3(b), we show the scaling of CE and forward emitted in-band energy with laser spot diameter, respectively, for a 23 ns main-pulse duration. The spot diameters are averaged over the major and minor axes of the 50% intensity contour. The CE is observed to increase at laser diameters of $\sim 70\text{ }\mu\text{m}$, which is a reflection of the higher enclosed energies of the larger beams close to the imaging plane. Experimental

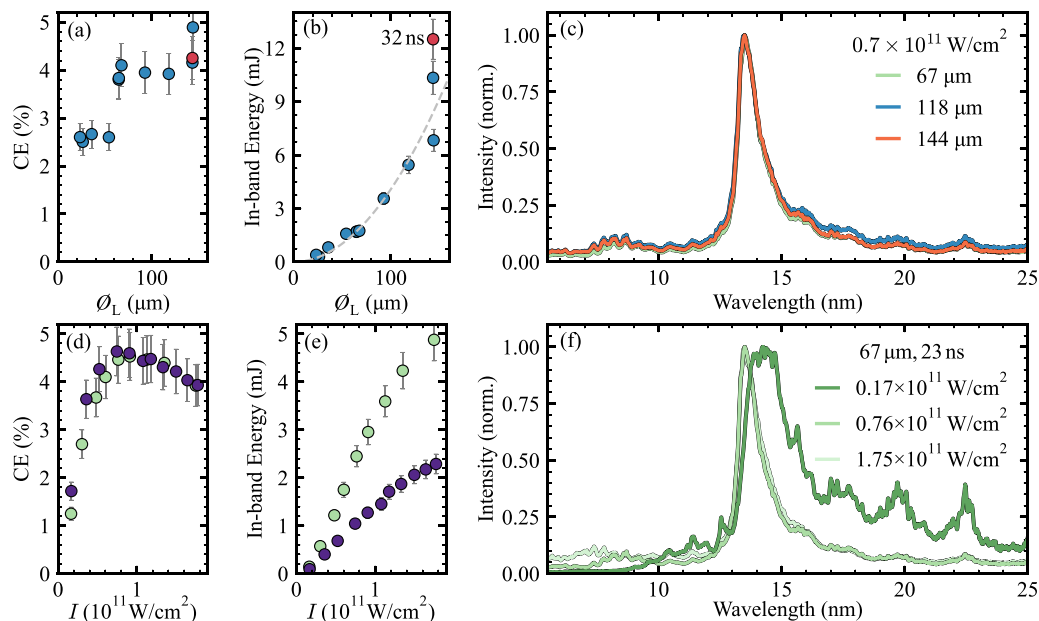


FIG. 3. Scaling of emitted EUV energy for tin targets that are much larger than the beam size. (a) The CE obtained for different laser beam spot sizes for 23 ns (●) and 32 ns (●) pulse durations. (b) The total emitted in-band EUV energy, in the hemisphere toward the laser, of the LPP as a function of the laser spot size. The gray dashed line indicates the $\sim \phi_L^2$ scaling (see main text). (c) EUV spectra in the range $5.5\text{--}25\text{ nm}$ for three different laser spot sizes under optimum intensity. (d) CE as a function of laser intensity for two pulse durations: 11 (●) and 23 ns (●) for a $67\text{ }\mu\text{m}$ beam diameter. (e) Total in-band energy for the two pulse duration cases under different illumination intensities. (f) EUV spectra for the 23 ns pulse duration case for three different laser intensities.

beam quality limitations result in different E_{end} for smaller beams and a resulting lower CE as previously discussed. The in-band energy emission scales approximately with the illumination area, i.e., as $\sim \phi_L^2$, reaching a value of 12.5 mJ for a 32 ns with 144 μm diameter. The spectra for three different beam diameters of 23 ns flat-top illumination at optimum intensity are shown in Fig. 3(c). We observe only minute differences in the spectra, which implies similar plasma opacity profiles and underlying plasma conditions such as temperature and density. This similarity in spectral emission across larger beam sizes is a result of optically thin plasma generation by 2 μm laser systems¹⁶ and allows for scaling the beam size without a loss in CE in this range.

In Fig. 3(d), the variation of CE with laser intensity is shown for two pulse duration cases of 11 and 23 ns, employing a 67 μm diameter beam. The two pulse durations result in a similar CE profile across a range of intensities, with their optimum at $0.7 \times 10^{11} \text{ W/cm}^2$. This value matches similarly established optimum intensities for solid and liquid tin targets.^{16,17} We note the slow decrease in CE with increasing laser intensity due to the slowly varying charge state with increasing temperature.³³ Such dependencies further allow for increasing in-band energy by increasing laser energy without significantly reducing CE. This possibility matches simulations under simplified conditions (without considering, e.g., target preshaping) in previous work.¹³ The scaling of the in-band energy with laser intensity is shown in Fig. 3(e). It is immediately clear that given the similarity in CEs in Fig. 3(d), the in-band energy scales linearly with laser pulse duration. Laser intensity changes lead to differences in emission spectra as shown for underheated, optimally heated, and overheated plasmas in Fig. 3(f). Although lower-than-optimum intensities underheating the tin plasma result in a broad spectrum, we observe small differences between the optimum and overheated spectra around the 13.5 nm regime. Major differences are only observed in the 6–10 nm range, which reflects information on the plasma ionic charge state composition and correspondingly, the plasma temperature.³⁴

We have thus created efficient, high energy, EUV emitting plasmas driven by 2 μm laser light and investigated the potential for further scaling of in-band energies. With careful control of the tin target, larger uniform-intensity laser profiles coupled with longer pulse durations and higher intensities, within the studied range, would provide even higher in-band energy emissions at high efficiency to power the nanolithographic process.

Given the importance of the emission source size for the lithographic process, we next study the source size in the radial (\hat{r}) and propagation directions (\hat{z}) of the laser beam as a result of scaling the in-band energy. For this purpose, images of the EUV emitting area are acquired at 90° [see Fig. 1(a)] and shown in Fig. 4(a) for a high CE case of a 67 μm diameter beam at optimum intensity with tin targets larger than the beam. The main-pulse laser propagates from left to right impacting the target (not visible). Similarly, for a high in-band energy emitting source (32 ns, 144 μm), an image of the significantly larger EUV emission area is shown in Fig. 4(b). In Fig. 4(c), we systematically study the source size as determined from its full width at 20% of maximum intensity along each (\hat{r} , \hat{z}) axis independently using the same data underlying Fig. 3. The 20% contour is chosen such that all reported sizes enclose a significant (>75%) fraction of the total emission energy. As expected, we observe that the source diameter increases with increasing laser spot size.²⁵ The gray line represents a linear fit to the data trend, with an offset of 21 μm attributed to plasma expansion.

The trend indicates a scale invariance of the emission, with a slope (of approximately $2.8\times$) attributed to the fact that (i) plasma is heated (through conduction but mostly via radiation transport¹³) well outside the laser absorption area and that (ii) significant laser energy is deposited outside [cf. Fig. 2(b)] of the area defining E_{end} , while (iii) the definitions of size of the (x , y) axes strongly differ—reducing the ϕ_{EUV} threshold to 50% is in fact found to reduce the fit slope to 1.5–2. Related to the above argument (ii), we indeed observe a notable downward deviation from the trend for the optimum CE case, due to a high E_{end} reducing the energy deposited outside ϕ_L . Here, we find that maximizing CE through E_{end} goes hand-in-hand with reducing emission source size.

We further examine the source size dependency on drive laser intensity for a spot size of 67 μm in Fig. 4(d). Higher intensities are observed to generate larger sources, similar to previous work,³⁵ primarily due to higher induced temperatures and charge states within the plasma, and increased plasma expansion rate—pushing the critical surface outward.¹³ The EUV emission size correspondingly increases. The observed increase is a complex function incorporating also the

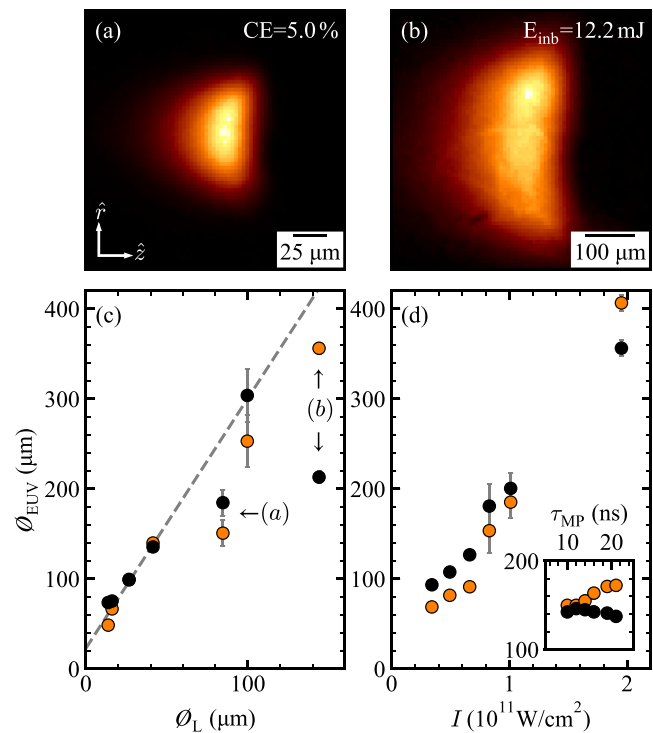


FIG. 4. Scaling of EUV source size (measured at 90°) with laser diameter and intensity. (a) Image of the EUV emission area for a maximum CE = 5.0% case. The laser propagates along the $+\hat{z}$ direction. (b) Image of the EUV emission area for high in-band emission (12.2 mJ). (c) Plasma source size ϕ_{EUV} as calculated by its full width at 20% of the maximum intensity along the \hat{r} (orange circles) and \hat{z} (black circles) directions as a function of laser spot size ϕ_L . All data points are acquired at a laser intensity of $0.7 \times 10^{11} \text{ W/cm}^2$. The gray dashed line indicates a trendline fit to the data. Data entries corresponding to the images in panels (a) and (b) are indicated. (d) Source size of a 67 μm laser beam with different intensities in the range $0.3\text{--}2 \times 10^{11} \text{ W/cm}^2$. Inset of (d) shows the scaling of source size with pulse duration in the range 10–23 ns. All the above-mentioned source sizes enclose $\geq 75\%$ of the EUV emission energy.

dependence of the EUV image on the CE [cf. Fig. 3(d)]. The inset to Fig. 4(d) shows the varying sizes with laser pulse durations under optimum intensity and beam diameters. We note that there is a much lower sensitivity of the source size with laser pulse duration. In fact, the multiplication $\phi_1 \times \phi_2$, yielding the emission area, is nearly independent of pulse length, allowing longer pulses and, thus, enabling higher in-band energy emission without significantly increasing the source size.

All presented source sizes match typically reported etendues.^{10,14} For example, an etendue of $3.3 \text{ mm}^2 \text{ sr}$ (number taken from Refs. 10 and 11) for a collector covering 5.5 sr of the forward hemisphere^{10,11} may be efficiently matched to a source size below approximately $600^2 \mu\text{m}^2$, assuming isotropic hemispherical emission. Of course, this view represents a strong simplification of the complex beam transport through the optical column through which EUV light is guided onto the wafer.

In conclusion, we have demonstrated highly efficient in-band EUV production from $2 \mu\text{m}$ -laser-generated plasma, obtaining a peak 5% conversion efficiency competitive with the industrial CO_2 -gas-laser powered state-of-the-art. Combined with the benefits of solid-state laser technology currently under development, in particular, with its promise of much larger (up to $\sim 20\%$, see Refs. 21 and 36) wall-plug efficiency, and laser pulse energy and power scalability,^{15,36} our findings make $2 \mu\text{m}$ -LPP a particularly promising candidate to power future EUV nanolithography machines. We further show the possibility to scale the extreme ultraviolet light emission toward high energies by studying output in-band energy scaling with laser spot size, intensity, and pulse duration. High in-band EUV energies of up to 12.5 mJ have been achieved, with scope for further scaling, while maintaining small emission source sizes match typical etendues of the EUV optics column. Further studies are required to optimize tin-target delivery, minimizing “debris” generation,^{10,37} including investigating the potential of further simplifying the plasma formation process.

We would like to thank Iliya Cerjak and Henk-Jan Boluijt for their work in designing the experimental setup and Laurens van Buuren for the aid in assembling the setup and its operation. We would like to further thank Ruben Schupp and Muharrem Bayraktar for their help with the experimental work as well as Lucas Poirier and Michael Purvis for helpful discussions. This research was funded by the European Research Council (ERC StG 802648) and the Dutch Research Council (Vidi 15697 and OTP 19458).

AUTHOR DECLARATIONS

Conflict of Interest

The authors have no conflicts to disclose.

Author Contributions

Yahia Mostafa and Lars Behnke contributed equally to this work.

Yahia Mostafa: Conceptualization (equal); Data curation (equal); Formal analysis (equal); Investigation (equal); Methodology (equal); Software (equal); Visualization (equal); Writing – original draft (equal); Writing – review & editing (equal). **Lars Behnke:** Conceptualization (equal); Data curation (equal); Formal analysis (equal); Investigation (equal); Methodology (equal); Visualization

(equal); Writing – original draft (equal); Writing – review & editing (equal). **Dion Junior Engels:** Data curation (equal); Investigation (equal); Writing – review & editing (equal). **Zoi Bouza:** Investigation (equal); Writing – review & editing (equal). **John Sheil:** Conceptualization (equal); Investigation (equal); Writing – review & editing (equal). **Wim Ubachs:** Conceptualization (equal); Supervision (equal); Writing – original draft (equal); Writing – review & editing (equal). **Oscar Oreste Versolato:** Conceptualization (equal); Funding acquisition (equal); Investigation (equal); Methodology (equal); Project administration (equal); Supervision (equal); Writing – original draft (equal); Writing – review & editing (equal).

DATA AVAILABILITY

The data that support the findings of this study are available from the corresponding author upon reasonable request.

REFERENCES

- M. Waldrop, *Nat. News* **530**, 144 (2016).
- J. van Schoot, K. Troost, F. Bornebroek, R. van Ballegoij, S. Lok, P. Krabbendam, J. Stoeldraijer, J. Benschop, J. Finders, H. Meiling, E. van Setten, B. Kneer, P. Kuerz, W. Kaiser, T. Heil, and S. Migura, *Proc. SPIE* **10583**, 105830R (2018).
- O. O. Versolato, J. Sheil, S. Witte, W. Ubachs, and R. Hoekstra, *J. Opt.* **24**, 054014 (2022).
- M. A. van de Kerkhof, F. Liu, M. Meeuwissen, X. Zhang, M. Bayraktar, R. C. de Kruijff, and N. V. Davydova, *J. Micro/Nanolithogr. MEMS MOEMS* **19**, 033801 (2020).
- A. Sasaki, A. Sunahara, H. Furukawa, K. Nishihara, S. Fujioka, T. Nishikawa, F. Koike, H. Ohashi, and H. Tanuma, *J. Appl. Phys.* **107**, 113303 (2010).
- G. O'Sullivan, B. Li, R. D'Arcy, P. Dunne, P. Hayden, D. Kilbane, T. McCormack, H. Ohashi, F. O'Reilly, P. Sheridan, E. Sokell, C. Suzuki, and T. Higashiguchi, *J. Phys. B* **48**, 144025 (2015).
- Q. Huang, V. Medvedev, R. van de Kruijs, A. Yakshin, E. Louis, and F. Bijkerk, *Appl. Phys. Rev.* **4**, 011104 (2017).
- F. Torretti, J. Sheil, R. Schupp, M. Basko, M. Bayraktar, R. Meijer, S. Witte, W. Ubachs, R. Hoekstra, O. Versolato, A. Neukirch, and J. Colgan, *Nat. Commun.* **11**, 2334 (2020).
- K. Kouge, S. Nagai, T. Hori, Y. Ueno, T. Yanagida, K. Miyao, H. Hayashi, Y. Watanabe, T. Abe, H. Nakarai, T. Saito, and H. Mizoguchi, *J. Photopolym. Sci. Technol.* **33**, 37 (2020).
- I. Y. Tolstikhina, S. Churilov, A. Ryabtsev, K. Koshelev, and V. Bakshi, *EUV Sources for Lithography* (SPIE Press, Bellingham, Washington, Oxford, 2006), Chap. 2.
- I. Fomenkov, D. Brandt, A. Ershov, A. Schafgans, Y. Tao, G. Vaschenko, S. Rokitski, M. Kats, M. Vargas, M. Purvis *et al.*, *Adv. Opt. Technol.* **6**, 173 (2017).
- Y. Nishimura, Y. Ueno, S. Nagai, F. Iwamoto, K. Miyao, H. Hayashi, Y. Watanabe, T. Abe, H. Nakarai, and H. Mizoguchi, *Proc. SPIE* **12051**, 120510T (2022).
- D. J. Hemminga, O. O. Versolato, and J. Sheil, *Phys. Plasmas* **30**, 033301 (2023).
- K. Tomita, Y. Pan, A. Sunahara, K. Kouge, H. Mizoguchi, and K. Nishihara, *Sci. Rep.* **13**, 1825 (2023).
- S. H. Langer, H. A. Scott, T. C. Galvin, E. S. Link, B. A. Reagan, and C. W. Siders, in EUVL Workshop, 2020.
- L. Behnke, R. Schupp, Z. Bouza, M. Bayraktar, Z. Mazzotta, R. Meijer, J. Sheil, S. Witte, W. Ubachs, R. Hoekstra, and O. O. Versolato, *Opt. Express* **29**, 4475 (2021).
- R. Schupp, L. Behnke, Z. Bouza, Z. Mazzotta, Y. Mostafa, A. Lassise, L. Poirier, J. Sheil, M. Bayraktar, W. Ubachs, R. Hoekstra, and O. O. Versolato, *J. Phys. D* **54**, 365103 (2021).
- R. Schupp, L. Behnke, J. Sheil, Z. Bouza, M. Bayraktar, W. Ubachs, R. Hoekstra, and O. O. Versolato, *Phys. Rev. Res.* **3**, 013294 (2021).
- Z. Y. Shi, Y. Yuan, W. P. Wang, Y. Y. Ma, X. Y. Sun, N. Lin, and Y. X. Leng, *Phys. Plasmas* **30**, 043107 (2023).

- ²⁰I. Tamer, B. A. Reagan, T. Galvin, J. Galbraith, E. Sistrunk, A. Church, G. Huete, H. Neurath, and T. Spinka, *Opt. Lett.* **46**, 5096 (2021).
- ²¹I. Tamer, B. A. Reagan, T. Galvin, F. Batysta, E. Sistrunk, D. Willard, A. Church, H. Neurath, J. Galbraith, G. Huete, and T. Spinka, *Opt. Express* **30**, 46336 (2022).
- ²²T. Sizyuk and A. Hassanein, *Phys. Plasmas* **27**, 103507 (2020).
- ²³M. Brandstätter, M. M. Weber, and R. S. Abhari, *J. Appl. Phys.* **129**, 233306 (2021).
- ²⁴Y. Yuan, Y. Y. Ma, W. P. Wang, S. J. Chen, Y. Cui, M. Zi, X. H. Yang, G. B. Zhang, and Y. X. Leng, *Plasma Phys. Controlled Fusion* **64**, 025001 (2021).
- ²⁵L. Yin, H. Wang, B. A. Reagan, C. Baumgarten, Z. Lyu, R. Soufli, E. Gullikson, V. N. Shlyaptsev, and J. J. Rocca, *IEEE Photonics J.* **13**, 1700115 (2021).
- ²⁶R. Schupp, F. Torretti, R. A. Meijer, M. Bayraktar, J. Sheil, J. Scheers, D. Kurilovich, A. Bayerle, A. A. Schafgans, M. Purvis, K. S. E. Eikema, S. Witte, W. Ubachs, R. Hoekstra, and O. O. Versolato, *Appl. Phys. Lett.* **115**, 124101 (2019).
- ²⁷L. Behnke, E. J. Salumbides, G. Görizt, Y. Mostafa, D. Engels, W. Ubachs, and O. Versolato, *Opt. Express* **31**, 24142 (2023).
- ²⁸J. Hernandez-Rueda, B. Liu, D. J. Hemminga, Y. Mostafa, R. A. Meijer, D. Kurilovich, M. Basko, H. Gelderblom, J. Sheil, and O. O. Versolato, *Phys. Rev. Res.* **4**, 013142 (2022).
- ²⁹Z. Bouza, J. Byers, J. Scheers, R. Schupp, Y. Mostafa, L. Behnke, Z. Mazzotta, J. Sheil, W. Ubachs, R. Hoekstra, M. Bayraktar, and O. O. Versolato, *AIP Adv.* **11**, 125003 (2021).
- ³⁰M. M. Basko, V. G. Novikov, and A. S. Grushin, *Phys. Plasmas* **22**, 053111 (2015).
- ³¹Z. Bouza, J. Scheers, A. Ryabtsev, R. Schupp, L. Behnke, C. Shah, J. Sheil, M. Bayraktar, J. R. C. López-Urrutia, W. Ubachs, R. Hoekstra, and O. O. Versolato, *J. Phys. B* **53**, 195001 (2020).
- ³²J. Filevich, J. J. Rocca, E. Jankowska, E. C. Hammarsten, K. Kanizay, M. C. Marconi, S. J. Moon, and V. N. Shlyaptsev, *Phys. Rev. E* **67**, 056409 (2003).
- ³³J. Sheil, O. O. Versolato, V. Bakshi, and H. A. Scott, "Review of the 1st EUV light sources code comparison workshop," *arXiv:2208.12699* (2022).
- ³⁴F. Torretti, R. Schupp, D. Kurilovich, A. Bayerle, J. Scheers, W. Ubachs, R. Hoekstra, and O. O. Versolato, *J. Phys. B* **51**, 045005 (2018).
- ³⁵A. Roy, G. Arai, H. Hara, T. Higashiguchi, H. Ohashi, A. Sunahara, B. Li, P. Dunne, G. O'Sullivan, T. Miura, T. Mocek, and A. Endo, *Appl. Phys. Lett.* **105**, 074103 (2014).
- ³⁶B. A. Reagan, I. Tamer, T. Galvin, F. Batysta, E. Sistrunk, D. Willard, A. Church, H. Neurath, J. Galbraith, G. Huete, C. Siders, S. Langer, and T. Spinka, in EUV Source Workshop, 2022.
- ³⁷O. O. Versolato, *Plasma Sources Sci. Technol.* **28**, 083001 (2019).